

TimeFlow: Longitudinal Brain Image Registration and Aging Progression Analysis

Bailiang Jian^{1,2,3}, Jiazhen Pan^{1,2}, Yitong Li^{1,3},
 Fabian Bongratz^{1,2,3}, Ruochen Li¹, Daniel Rueckert^{1,2,3,4},
 Benedikt Wiestler^{1,2,3*} and Christian Wachinger^{1,2,3*}

¹ Technical University of Munich, Germany

`bailiang.jian@tum.de`

² Klinikum Rechts der Isar, Munich, Germany

³ Munich Center for Machine Learning, Germany

⁴ Imperial College London, United Kingdom

Abstract. Predicting future brain states is crucial for understanding healthy aging and neurodegenerative diseases. Longitudinal brain MRI registration, a cornerstone for such analyses, has long been limited by its inability to forecast future developments, reliance on extensive, dense longitudinal data, and the need to balance registration accuracy with temporal smoothness. In this work, we present *TimeFlow*, a novel framework for longitudinal brain MRI registration that overcomes all these challenges. Leveraging a U-Net architecture with temporal conditioning inspired by diffusion models, TimeFlow enables accurate longitudinal registration and facilitates prospective analyses through future image prediction. Unlike traditional methods that depend on explicit smoothness regularizers and dense sequential data, TimeFlow achieves temporal consistency and continuity without these constraints. Experimental results highlight its superior performance in both future timepoint prediction and registration accuracy compared to state-of-the-art methods. Additionally, TimeFlow supports novel biological brain aging analyses, effectively differentiating neurodegenerative conditions from healthy aging. It eliminates the need for segmentation, thereby avoiding the challenges of non-trivial annotation and inconsistent segmentation errors. TimeFlow paves the way for accurate, data-efficient, and annotation-free prospective analyses of brain aging and chronic diseases.

1 Introduction

Understanding how the human brain changes over time — both in the course of healthy aging and under the influence of neurodegenerative diseases — remains a central challenge in neurology and related fields [33,34]. Such insights not only shed light on the underlying pathological processes but also pave the way for more individualized treatment planning and earlier, more targeted interventions [6]. Magnetic Resonance (MR) imaging has become the standard modality

* Equal Advising

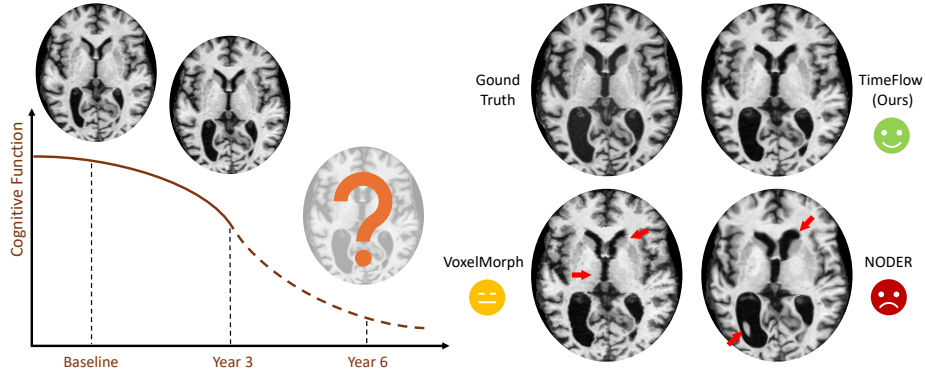


Fig. 1. Comparative performance of *TimeFlow* for future brain MRI prediction. *TimeFlow* demonstrates the superior capability of future extrapolation compared to (i) NODER, which employs NeuralODE for geodesic regression, and (ii) VoxelMorph with linear scaling. Given two previous timepoints (baseline and Year 3), *TimeFlow* can extrapolate precise and smooth deformation to predict brain MRI in Year 6.

for capturing these longitudinal changes, owing to its high spatial resolution and excellent soft-tissue contrast. By repeatedly scanning the same individual, clinicians and researchers can visualize evolving patterns of atrophy, lesion progression, and other structural transformations as they unfold [20,2].

At the core of analyzing these changes lies longitudinal registration [16,43], which aligns a subject’s brain images across multiple time points to quantify subtle, subject-specific anatomical alterations. While retrospective assessment of these changes is valuable, the ability to predict future brain transformations is even more critical [27]. Accurate predictions can inform clinicians about impending disease progression and help them forecast trajectories of atrophy, ultimately guiding more effective interventions [23].

However, current longitudinal registration approaches fall short when it comes to predicting future changes [50,3,51], as illustrated in Fig. 1. They generally focus on modeling the observed sequence of scans, allowing interpolation between known time points but lacking the capability to extrapolate beyond the final scan. Many methods also require densely sampled longitudinal data, often more than five scans [28,36], which is impractical in typical clinical scenarios since usually one or a few follow-up scans (<3) are acquired. Finally, existing frameworks frequently impose temporal smoothness constraints [49,53,42], which can degrade spatial registration accuracy, necessitating a careful balance between smoothness and accuracy.

We introduce *TimeFlow*, a novel longitudinal brain MRI registration designed for predicting future brain changes. The key contribution is a novel constraint

that ensures temporal consistency and continuity — removing the demand for explicit smoothness regularizers. Moreover, TimeFlow can operate longitudinal registration with only paired images in inference, eliminating the requirement for long image sequences. Finally, TimeFlow can extrapolate to future time points and analyze aging progression without relying on segmentation masks. Our contributions are twofold:

1. Inspired by conditioning mechanisms used in diffusion models, TimeFlow employs a U-Net architecture conditioned on a temporal parameter reflecting biological aging. This temporal conditioning allows for generating **temporally continuous and smooth deformation fields, even when only two images are used as input**. Moreover, this approach enables the prediction of future-timepoint images, outperforming current state-of-the-art methods in extrapolating future brain images.
2. We develop a novel methodology for longitudinal brain aging and disease progression analysis, utilizing TimeFlow’s advanced predictive capabilities. Our approach **quantifies relative aging progression using healthy subjects as a reference baseline**, where biological aging is assumed to align with chronological aging. This method enables the identification and differentiation of subjects with Mild Cognitive Impairment (MCI) and Dementia, who typically exhibit accelerated biological aging compared to chronological aging. Remarkably, our method performs this analysis solely through registration, eliminating the need for brain structure annotations and avoiding potential segmentation-related error propagation.

2 Related Work

Cross-sectional registration methods laid the groundwork for medical image registration, pioneering this field with techniques such as parametric spline-based models [41,29], optical flow [35,52], and diffeomorphic transformations [44,47,5]. However, they demand prohibitive computing time in the order of several ten-minute to register one single pair of images, posing a significant barrier to clinical deployment. To address this, learning-based frameworks [4,31,37,7,13,21] have emerged, dramatically reducing inference time and often improving registration accuracy. More recently, diffusion-model-based approaches have demonstrated remarkable generative capabilities, further enhancing registration performance [22,54]. Nevertheless, all such methods rely on carefully tuned smoothness regularizers to ensure anatomically plausible deformation fields. An improper weighting factor of smoothness regularizers can either reduce fidelity or introduce unrealistic warps. Additional tuning or adaptive strategies are often needed to strike an optimal balance [17,32,48].

Longitudinal registration methods [42,19,18,11,10,36,9,24] often leverage the backbone architecture of the cross-sectional registration, whereas one additional constraint is introduced: the temporal continuity/consistency across multiple

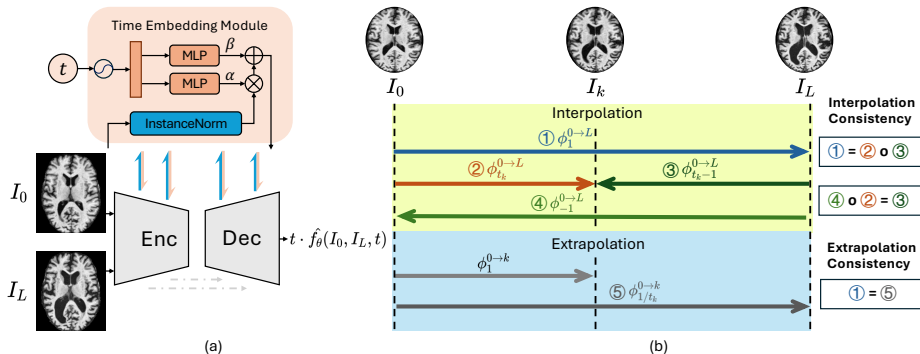


Fig. 2. (a) Architecture of *TimeFlow*. The U-Net \hat{f}_θ integrates time t information via adaptive instance normalization. The network takes the time t , the images at first ($t = 0$) and last visit ($t = L$) as input, generating comprehensive temporal deformations. (b) **Interpolation** and **Extrapolation** Consistency. *TimeFlow* can predict bidirectional time-continuous deformation fields. The symmetric intermediate similarity forces the deformed images to be aligned at time t_k , while the intermediate interpolation flow constraint encourages the deformation composition consistency. The extrapolation similarity and flow enforcement give information on what a realistic and reasonable extrapolation should be. Training with both consistency losses enables *TimeFlow* to generate plausible deformation in $t \in [-\infty, +\infty]$.

timepoints of a subject. Two major strategies are often used to tackle this problem. First, an explicit smoothness constraint along the temporal dimension is incorporated to maintain coherent deformation fields over time [53,28]. However, as with spatial smoothness, temporal regularization faces a similar trade-off: enforcing temporal continuity can inadvertently lower spatial accuracy. Second, many longitudinal methods require multiple, densely sampled scans (>10) to capture temporal dynamics [3,50]. In real-world clinical scenarios, patients often have only a few follow-up scans (≤ 3), restricting model flexibility and practical implementation. Importantly, these methods commonly can only carry out retrospective analyses and are not capable of prospective studies such as future image extrapolation and aging/disease progression risk prediction.

3 Methods

3.1 Time-Continuous Registration

Given a sequence of longitudinal images $\{I_k \mid k = 0, \dots, L\}$, we aim to find a temporally continuous deformation trajectory that connects all the discrete time points. To achieve this, we construct a time-continuous registration function $\phi_t = f_\theta(I_0, I_L, t)$. It takes the first visit I_0 and the last visit I_L as input images and predicts the deformation ϕ_t at time t . As shown in Figure 2, we utilize a time-embedded UNet, frequently used in diffusion models [14,40] to learn the mapping

function. The time variable t is first projected to the latent embedding space by a sinusoidal positional encoding layer and two-layer MLPs. Next, the time latent vector is fed to two separate MLPs to steer the mean and variance of the inter-layer adaptive instance normalization. The network is thus instilled with the capability of generating meaningful time embedding and predicting time-continuous flow fields by the novel time conditioning mechanism. Moreover, to ensure the predicted deformation trajectory passes through each visit I_k at time $t = t_k$, we incorporate the intermediate time points as supervision in training.

3.2 Interpolation Constraints

Intermediate Similarity. Our goal is to learn a time-continuous registration function $\phi_t^{0 \rightarrow L} = f_\theta(I_0, I_L, t)$. When $t = 0$, we have $f_\theta(I_0, I_L, 0) = \text{Id}$, the identity mapping. When $t \in (0, 1]$, $\phi_t^{0 \rightarrow L}$ is the forward deformation mapping from I_0 towards I_L , and $\phi_1^{0 \rightarrow L}$ moves I_0 to reach I_L . Similarly, for negative values, $t < 0$, ϕ_t maps backward from I_L to I_0 . Exploiting bidirectional time-continuous deformations, we can formulate a symmetric similarity measure:

$$\mathcal{L}_{\text{sim}}(I_0 \circ \phi_{t_k}^{0 \rightarrow L}, I_k) + \mathcal{L}_{\text{sim}}(I_L \circ \phi_{t_k-1}^{0 \rightarrow L}, I_k), \quad (1)$$

which deforms both images to remove the bias introduced by single-side warping [1,30,15]. As shown in the upper green part in Figure 2(b), $I_0 \circ \phi_{t_k}^{0 \rightarrow L}$ and $I_L \circ \phi_{t_k-1}^{0 \rightarrow L}$ describe the deformations of I_0 and I_L to the time $t = t_k$. Given an acquired MRI I_k at time $t = t_k$, we can simply use it to compute the symmetric intermediate similarity and thus force the network to learn plausible deformation trajectories from I_0 to I_L that pass through intermediate images.

Generalized Intermediate Similarity. However, in real-world clinical scenarios, many subjects will only have MRI from two time points available. In such a case, we rewrite the symmetric similarity as:

$$\mathcal{L}_{\text{sim}}(I_0 \circ \phi_{\hat{t}}^{0 \rightarrow L}, I_L \circ \phi_{\hat{t}-1}^{0 \rightarrow L}), \quad (2)$$

where \hat{t} is sampled from a uniform distribution $\mathcal{U}(0, 1)$. The registration is guided properly through this synthetic variant of the symmetric similarity, even without any intermediate observation as supervision. Moreover, taking advantage of the freedom to choose \hat{t} , the network can learn densely on the time axis and is no longer constrained to intermediate visits at specific times in the dataset.

Interpolation Consistency. To encourage plausible time-continuous deformations, we propose the interpolation consistency as a regularizer:

$$\mathcal{L}_{\text{inter-consis}} = \|\phi_1^{0 \rightarrow L} \circ \phi_{t_k-1}^{0 \rightarrow L} - \phi_{t_k}^{0 \rightarrow L}\|_2^2 + \|\phi_{-1}^{0 \rightarrow L} \circ \phi_{t_k}^{0 \rightarrow L} - \phi_{t_k-1}^{0 \rightarrow L}\|_2^2, \quad (3)$$

which combines the two constraints formulated in Figure 2(b). We formulated the loss with the notation t_k , but as described in the previous paragraph, t_k can also be sampled from the uniform distribution if no intermediate observation

exists. It is derived from the common transformation composition consistency that two consecutive transforms are equivalent to a direct transform. Moving from $t = 0$ to $t = 1$ and then back to $t = t_k$ is equivalent to moving directly from $t = 0$ to $t = t_k$. It is worth noting that this differs from the commonly used smoothness regularizations, which explicitly enforce a smooth gradient over the flow field. Therefore, there is only a minimal trade-off between accuracy and smoothness since both the similarity and the flow consistency encourage plausible and reasonable longitudinal transformations.

3.3 Extrapolation Consistency

Through the intermediate similarity and interpolation consistency, we obtain meaningful predictions for bidirectional registrations in $t \in [-1, 1]$. As our main objective is extrapolation, we formulate criteria for the intervals $[1, +\infty)$ (forward) and $(-\infty, -1]$ (backward) next. To this end, we consider the deformation $\phi_1^{0 \rightarrow k}$ from I_0 to I_k . Given the time of I_k being t_k , it holds that $\phi_{t_k}^{0 \rightarrow L} = \phi_1^{0 \rightarrow k}$, as illustrated in Figure 2(b). Consequently, we can then formulate $\phi_1^{0 \rightarrow L} = \phi_{1/t_k}^{0 \rightarrow k}$, where $\phi_{1/t_k}^{0 \rightarrow k}$ denotes an extrapolation because $t_k \in (0, 1)$ and therefore $1/t_k > 1$. Based on this notation, we define the *extrapolation similarity* as:

$$\mathcal{L}_{\text{sim}}(I_0 \circ \phi_{1/t_k}^{0 \rightarrow k}, I_L). \quad (4)$$

Again, we can either use intermediate observations with time t_k or sample from $\mathcal{U}(0, 1)$. If t_k is sampled from $\mathcal{U}(0, 1)$, i.e., I_k is not observed but only I_0 and I_L , we then define $I_k = I_0 \circ \phi_{t_k}^{0 \rightarrow L}$. In addition to the extrapolation similarity measure, we define the forward *extrapolation consistency* as:

$$\mathcal{L}_{\text{ext-consis}} = \|\phi_1^{0 \rightarrow L} - \phi_{1/t_k}^{0 \rightarrow k}\|_2^2. \quad (5)$$

As shown in the bottom grey part of Figure 2(b), both $\phi_1^{0 \rightarrow L}$ and $\phi_{1/t_k}^{0 \rightarrow k}$ map from I_0 to I_L , thus should be consistent with each other. The backward versions of the extrapolation similarity and extrapolation consistency are:

$$\mathcal{L}_{\text{sim}}(I_L \circ \phi_{1/(t_k-1)}^{k \rightarrow L}, I_0) \quad \text{and} \quad \mathcal{L}_{\text{ext-consis}} = \|\phi_{-1}^{0 \rightarrow L} - \phi_{1/(t_k-1)}^{k \rightarrow L}\|_2^2. \quad (6)$$

The similarity measures and flow consistencies both contribute to achieving a realistic and coherent extrapolation. The proposed losses effectively ensure accurate extrapolation while implicitly capturing temporal consistency and continuity, without the need for additional temporal smoothness constraints.

4 Data and Experiments

Data and Pre-processing. We evaluate our method on the public Alzheimer’s Disease Neuroimaging Initiative (ADNI) dataset, which comprises longitudinal T1-weighted Magnetic Resonance (MR) scans from both healthy subjects and

patients diagnosed with Alzheimer’s Disease (AD) or MCI, i.e., neurodegenerative disorders that exhibit specific patterns of atrophy development in the brain. We employ the longitudinal processing from FreeSurfer v7.2 [12]. First, all scans are processed individually, including skull stripping, normalization. Subsequently, the image sequence is rigidly aligned via a groupwise rigid registration [39]. FreeSurfer aggregates information across time points and refines the pre-processed outputs. We first select 134 subjects who underwent substantial anatomical change (median change magnitude within the brain is $> 0.3\text{mm}$) over time. Then, the dataset is divided into training, validation, and testing sets, ensuring a balance in diagnosis, age, sex, and the number of visits. It results in 74, 30, 30 subjects for each split, respectively, with the number of time points per subject ranging from 2 to 12. All input scans have isotropic 1mm spacing and are cropped to a uniform size of $160 \times 160 \times 192$ voxels. The intensity values are scaled to the range $[0,1]$, from percentile $[0,99.9]$ without clipping.

Implementation Details. Our model is implemented using Pytorch 2.1.2. and training/test is carried out on one NVIDIA A100 40G with a batch size of 1. We set the dimension of time embedding to 16, the feature channels in the U-Net encoder and decoder to $[32, 32, 48, 48, 96]$. In addition to TimeFlow, which outputs the time-dependent deformation field directly, we have the diffeomorphic variant TimeFlow_{diff}, which utilizes the *scaling and squaring* layer with 7 integration steps to integrate the temporal stationary velocity field. The weights of both interpolation and extrapolation similarity are set to 1.0. The weights of interpolation and extrapolation flow consistency are set to 2, 0.03 for TimeFlow and 1.25, 0.025 for TimeFlow_{diff}.

Baselines. To evaluate the registration performance we compare TimeFlow with the following methods:

- NODER [51,3], which is aware of every time point and takes the complete image sequence as the model input. It carries out subject-specific optimization and models the time-varying velocity field with a neural network and leverages Neural ordinary differential equation (ODE) [8] to compute integration and adjoint gradients. It fits the subject-specific temporal deformation trajectory by maximizing the similarity with each frame.
- VoxelMorph (VXM) [4] and the extended diffeomorphic VoxelMorph (VXM_{diff}) employing scaling and squaring. Since both VXM/VXM_{diff} are pairwise registration methods, the interpolation and extrapolation prediction is carried out based on the linear scaling of the displacement or velocity field from the pairwise registration.
- Sequence-based VoxelMorph (Seq-VXM) [50]. Seq-VXM processes the whole sequence and registers the baseline/endpoint images to each intermediate time point. Given that Seq-VXM performs multiple pairwise registrations by taking the whole image sequence as model input, it is also aware of all images at every time point. Therefore, we treat Seq-VXM as the *performance upper bound* for the retrospective study (refer to Table 2).

For all learning-based methods, we apply Local Normalized Cross Correlation (LNCC) as the training loss, the same as in TimeFlow. The radius of LNCC in NODER is set to $r = 9$ while for the other methods, it is set to $r = 4$. The loss function weighting factors in NODER follows their original suggestion, while Seq-VXM, VXM and VXM_{diff} compute the SOTA smoothness regularizer GradICON [46,45] with weight 1.5, 0.5, 1.0.

Evaluation metrics. In this work, we do NOT use Dice score to evaluate the longitudinal registration for the following two reasons: First, the most severe anatomical changes over time within the same subject are still relatively small compared to inter-subject registration. Second, the automatic annotations by Freesurfer are longitudinally inconsistent [38]. The label noise actually overshadows the true longitudinal differences based on our observation. Hence, using the Dice score cannot effectively reflect the nuanced but relevant structural change across time. Therefore, we use intensity-based instead of segmentation-based metrics to evaluate the registration. We use mean absolute error (MAE) and peak signal-to-noise ratio (PSNR) to quantitatively evaluate the image alignment and the standard deviation of the logarithm of the Jacobian determinant (SDlogJ) [25] and Non-diffeomorphic Volume (NDV) [26] to measure irregular volume change during registration and assess the plausibility of the deformation fields. All metrics are only applied in the foreground brain area.

5 Results

5.1 Prospective studies: Predicting the future

We first evaluate TimeFlow’s performance in prospective studies, i.e., for predicting follow-up images. Our model can perform this prospective analysis in two ways: 1. Based on two available scans and given a future timepoint t ($t > 1$), our model can directly predict the extrapolated image at this timepoint. 2. Given a future scan, our model can estimate the corresponding t , which can reflect the subjects’ biological aging progression.

Given t , predict the future image. As discussed in the method, one of TimeFlow’s biggest benefits is its ability to naturally extrapolate and predict a future image given $t > 1$. The quantitative evaluation of extrapolation is showcased in Table 3. TimeFlow demonstrates superior extrapolation accuracy compared to all baselines with the lowest MAE and the highest PSNR. Seq-VXM is not compared here since it cannot carry out future predictions. Figure 3 (Year 8) and Figure 4 illustrate TimeFlow’s extrapolation prediction when ground truth images are available, while Figure 5 demonstrates the extrapolation given a large t where ground truth is not available anymore. In all three figures, superior predictions of TimeFlow can be observed, with the least remaining errors compared to baselines, and it also shows more realistic extrapolations, whereas the baseline methods in Figure 5 fail.

Metrics	rigid	NODER	VXM	VXM-diff	TimeFlow	TimeFlow-diff
MAE ↓	10.3±1.9	9.3±1.9	9.1±1.9	9.2±2.0	8.6±1.6	8.8±1.8
PSNR ↑	16.9±1.5	18.0±1.7	18.3±1.9	18.4±1.9	18.8±1.7	18.7±1.9
SDlogJ ↓	-	1.8±0.9	6.3±4.8	6.3±2.0	5.0±1.0	6.0±1.0
NDV ↓	-	0.2±1.9	10 ⁴ ± 10 ⁴	10 ³ ± 10 ³	10 ³ ± 10 ³	6.1±11.2

Table 1. Comparative extrapolation evaluation of baselines and *TimeFlow/-diff* in terms of MAE (in scale $\times 10^{-2}$), PSNR, SDlogJ (also $\times 10^{-2}$) and non-diffeomorphic volume (NDV) in the foreground. Methods with the subscript _{diff} use the *scaling and squaring* method to integrate the SVF. The best score is marked in bold.

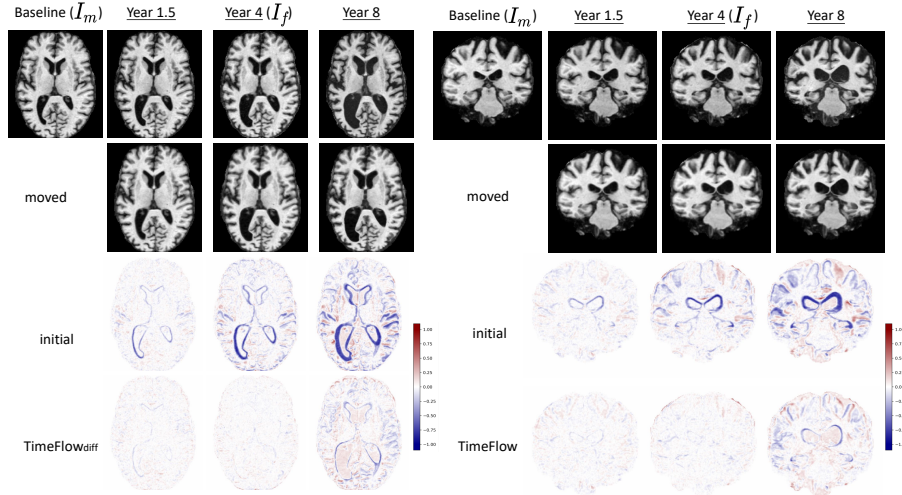


Fig. 3. Visualization of the Interpolation/Extrapolation Results. *TimeFlow/-diff* takes the baseline and Year 4 images as input, interpolates to Year 1.5, and extrapolates to Year 8. The first row displays the original images. The second row shows the warped baseline image. The third row presents the subtraction (error) map between the target and moved images. The value is in the range $[-1, 1]$, since the image intensities are normalized to $[0, 1]$. The visualization demonstrates that *TimeFlow/-diff* achieves high accuracy in both temporal interpolation and extrapolation.

Given future scan, assess the brain aging. We can utilize the extrapolation capability of TimeFlow for disease progression analysis. For each given future scan, we can predict a corresponding t value. We compare the relative brain aging rate of each diagnosis group in ADNI, i.e., Controls, MCI and Dementia. Specifically, we sample MRI triplets of time points with similar year intervals in between from the validation and test set. Then, we apply the first two time points as input and extrapolate to the third, future time point. By comparing with the ground truth MRI, we compute the optimal extrapolated time t_{ext} to match it. From this, we can compute the brain aging rate by dividing the extrapolated time by the actual time interval. The idea is that if brain aging is accelerated, i.e., in MCI or Dementia patients, the progression rate will be larger than 1.0,

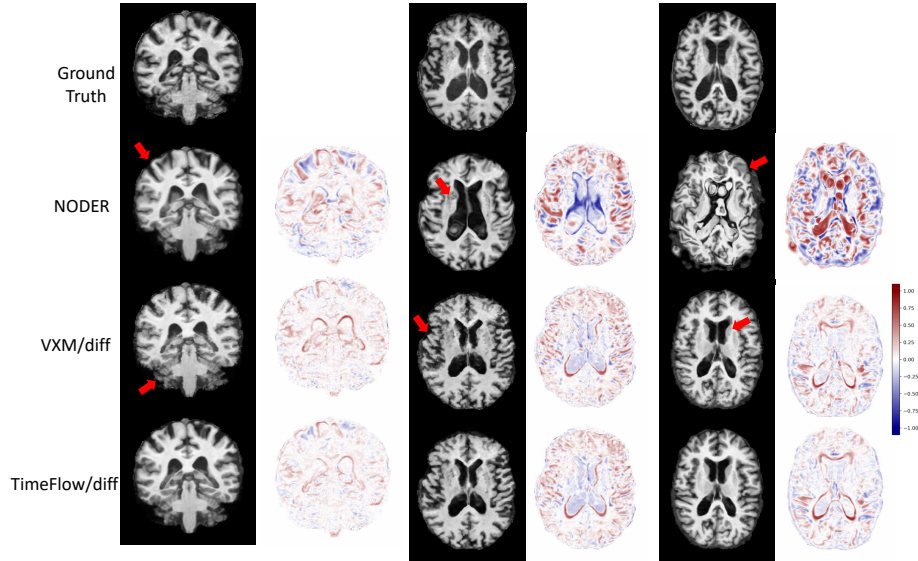


Fig. 4. Visualization of the Extrapolation Results. The extrapolation results predicted by the methods are compared with the ground truth future timepoint. The bottom two rows of the second and third columns present the diffeomorphic variants: VXM_{diff} , $TimeFlow_{\text{diff}}$. Major flaws are pointed out with red arrows. The deformation predictions of VXM_{diff} are not smooth and dissolve the brain (zoom-in for more details).

meaning that brain aging is faster than chronological aging. As shown in the box-plot of Figure 6, Dementia indeed has the highest progression rate, with MCI the second, while the control group is close to 1, highlighting a biologically plausible separation of groups based on our brain aging rate metric. To visualize the brain aging rate over time, we plot subject-specific progression curves for 9 representative subjects (three from each group). We observe a clear pattern, where both MCI and Dementia have accelerated progression compared to the baseline visit while control group (CN) maintains a more flat curve. This highlights how the extrapolation capacity of TimeFlow enables meaningful prospective analysis on Alzheimer’s disease, without the demand for extra anatomical annotations.

5.2 Retrospective studies: Matching the deformation trajectory

We carry out further studies with image interpolation to assess if plausible deformation fields are learned by TimeFlow. In this scenario, the first scan I_0 and the last scan I_L are available, and we want to estimate the deformation field to register the intermediate image I_k , with $0 < k < L$. The quantitative comparison to the baseline methods is shown in Tab. 2. As already mentioned in section 4, Seq-VXM takes the whole sequence as input and carries out explicit pairwise registration for each pair in the sequence. Consequently, it is regarded as the performance upper bound (“Oracle”) here. Although Timeflow only takes

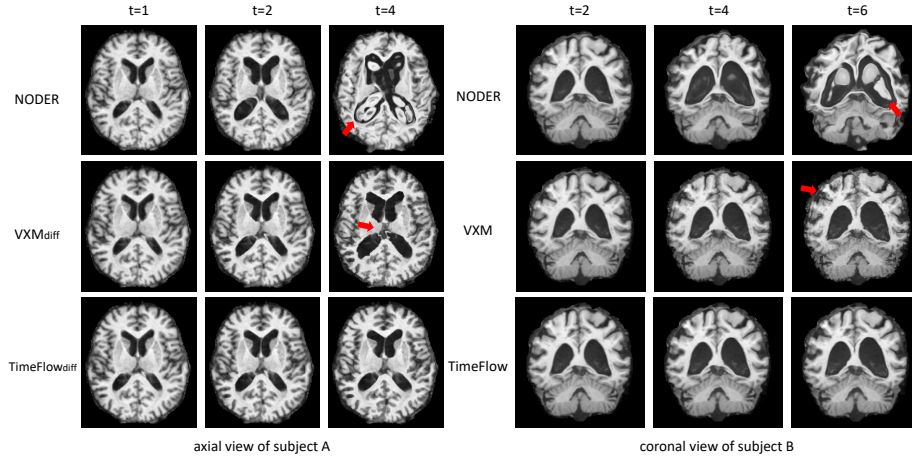


Fig. 5. Visualization of the Extrapolation Prediction. All methods predict extrapolated time points using the baseline and the endpoint as input. The figure shows the axial view of subject *A*'s registration result at $t = 1$ and extrapolation results at $t = 2, 4$, as well as the coronal view of subject *B*'s extrapolation results at $t = 2, 4, 6$. The major prediction flaws are highlighted.

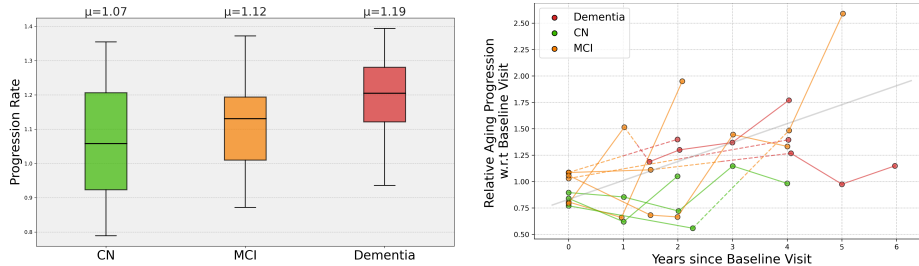


Fig. 6. Left: Progression Analysis for Control (CN), MCI and Dementia. The closer the progression rate to 1, the slower the pathological brain structural change is. Right: Relative Progression of 9 representative subjects. Each colored dot represents one visit. The x -axis denotes the years since the first visit. The y -axis stands for the relative progression rate compared to the baseline visit. The larger the number, the faster the brain structural changes. The grey line in the background is the mean fitted linear line across subjects. The colormap: CN-green, MCI-orange, Dementia-red.

the first and last scan as input, it achieves superior results to NODER, which is aware of the whole sequence and parametrized by Neural ODE. TimeFlow_{diff} demonstrates the least non-diffeomorphic volume without any extra smoothness regularization. The qualitative evaluation of the interpolation is shown in Fig. 3

(Year 1.5). In both cases, TimeFlow demonstrates satisfactory registration with almost no residual errors remaining compared to the initial errors.

Metrics	Seq-VXM (Upper bound)	rigid	NODER	VXM	VXM-diff	TimeFlow	TimeFlow-diff
MAE ↓	4.5±1.4	7.3±1.1	5.5±0.9	5.6±1.1	5.5±1.0	5.5±1.0	5.3±1.0
PSNR ↑	25.2±2.4	20.6±1.5	23.2±1.5	22.9±1.7	23.2±1.7	23.0±1.7	23.3±1.8
SDlogJ ↓	2.6±0.5	-	1.8±0.5	1.5±0.2	2.2±0.3	1.6±0.1	2.2±0.2
NDV ↓	0.0±0.1	-	0.0±0.3	0.2±0.4	0.1±0.2	0.1±0.4	0.0±0.0

Table 2. Comparative interpolation results of baselines and *TimeFlow/-diff* to evaluate the ability of deformation trajectory matching. *Seq-VXM* serves as the performance upper bound that performs multiple pairwise registrations between the baseline and midpoints. The best score is marked in bold.

6 Discussion and Conclusion

Novelty. TimeFlow introduces novel interpolation and extrapolation constraints that ensure temporal consistency without explicit smoothness regularizer. Together with the time-conditioning mechanism inspired by diffusion models, this enables effective extrapolation beyond the observed time frame. While we have used UNet as the base model, our contributions are generic and can, therefore, also be integrated into other registration backbones. Importantly, TimeFlow has significant application potential in areas such as in-silico drug effectiveness analysis. By extrapolating brain images to future timepoints at the beginning of a treatment, the predicted outcomes can be compared with actual follow-up scans. Discrepancies between predicted and observed results may then be attributed to treatment effects, offering a novel and efficient approach for evaluating therapeutic efficacy in clinical settings.

Limitation and failure cases. TimeFlow encounters challenges in the following two scenarios: 1. Future image prediction/aging progression analysis with minimal biological aging differences: When the two base input images are temporally close and exhibit no noticeable aging differences, TimeFlow struggles to predict future images effectively based on them. In such cases, the two input images collapse into a single timepoint, rendering the model incapable of extrapolation based on a “single” input data. 2. Prediction for large time intervals: Although TimeFlow is designed to estimate future images for any given time parameter $t \in [0, \infty]$, its performance deteriorates for large t values e.g. $t > 6$. This limitation is expected due to the insufficient availability of long-range temporal data in the ADNI dataset, meaning TimeFlow rarely encountered such scenarios during training, and, of course, the fact that modeling such long developments, which are influenced by a plethora of parameters, is inherently very challenging.

Conclusion. In this work, we introduced TimeFlow, a novel framework for longitudinal brain MR registration that addresses key challenges in the field, including the trade-off between accuracy and temporal consistency, limited temporal data, and the incapability of prospective predictions. By leveraging a simple yet effective combination of a UNet and temporal condition embedding, TimeFlow eliminates the need for smoothness terms, achieves accurate registration using only paired images, and most importantly, enables future image prediction and aging progression analysis without reliance on segmentation. Experimental results demonstrate its superior performance in both registration and prediction tasks, offering a powerful tool for advancing brain aging and neurodegenerative disease research. TimeFlow sets a foundation for future exploration into efficient, annotation-free, and predictive analyses in longitudinal imaging.

Acknowledgments. This work was supported by BMWi (project “NeuroTEMP”) research funding and the Munich Center of Machine Learning (MCML). Jiazhen Pan is funded by the European Research Council (ERC) project Deep4MI (884622).

Disclosure of Interests. The authors declare no competing interests.

References

1. Avants, B.B., Epstein, C.L., Grossman, M., Gee, J.C.: Symmetric diffeomorphic image registration with cross-correlation: evaluating automated labeling of elderly and neurodegenerative brain. *Medical image analysis* **12**(1), 26–41 (2008)
2. Baheti, B., Waldmannstetter, D., Chakrabarty, S., Akbari, H., Bilello, M., Wiestler, B., Schwarting, J., Calabrese, E., Rudie, J., Abidi, S., et al.: The brain tumor sequence registration challenge: establishing correspondence between pre-operative and follow-up mri scans of diffuse glioma patients. *arXiv preprint arXiv:2112.06979* (2021)
3. Bai, H., Hong, Y.: Noder: Image sequence regression based on neural ordinary differential equations. In: *International Conference on Medical Image Computing and Computer-Assisted Intervention*. pp. 673–682. Springer (2024)
4. Balakrishnan, G., Zhao, A., Sabuncu, M.R., Guttag, J., Dalca, A.V.: Voxelmorph: a learning framework for deformable medical image registration. *IEEE transactions on medical imaging* **38**(8), 1788–1800 (2019)
5. Beg, M.F., Miller, M.I., Trounev, A., Younes, L.: Computing large deformation metric mappings via geodesic flows of diffeomorphisms. *International journal of computer vision* **61**, 139–157 (2005)
6. Breijyeh, Z., Karaman, R.: Comprehensive review on alzheimer’s disease: causes and treatment. *Molecules* **25**(24), 5789 (2020)
7. Chen, J., Frey, E.C., He, Y., Segars, W.P., Li, Y., Du, Y.: Transmorph: Transformer for unsupervised medical image registration. *Medical image analysis* **82**, 102615 (2022)
8. Chen, R.T., Rubanova, Y., Bettencourt, J., Duvenaud, D.K.: Neural ordinary differential equations. *Advances in neural information processing systems* **31** (2018)
9. Csapo, I., Davis, B., Shi, Y., Sanchez, M., Styner, M., Niethammer, M.: Longitudinal image registration with temporally-dependent image similarity measure. *IEEE transactions on medical imaging* **32**(10), 1939–1951 (2013)

10. Dong, M., Xie, L., Das, S.R., Wang, J., Wisse, L.E., deFlores, R., Wolk, D.A., Yushkevich, P.A.: Regional deep atrophy: Using temporal information to automatically identify regions associated with alzheimer’s disease progression from longitudinal mri. *Imaging Neuroscience* **2**, 1–23 (2024)
11. Dong, M., Xie, L., Das, S.R., Wang, J., Wisse, L.E., DeFlores, R., Wolk, D.A., Yushkevich, P.A., Initiative, A.D.N., et al.: Deepatrophy: Teaching a neural network to detect progressive changes in longitudinal mri of the hippocampal region in alzheimer’s disease. *Neuroimage* **243**, 118514 (2021)
12. Fischl, B.: Freesurfer. *Neuroimage* **62**(2), 774–781 (2012)
13. Ghahremani, M., Khateri, M., Jian, B., Wiestler, B., Adeli, E., Wachinger, C.: H-vit: A hierarchical vision transformer for deformable image registration. In: *Proceedings of the IEEE/CVF Conference on Computer Vision and Pattern Recognition*. pp. 11513–11523 (2024)
14. Ho, J., Jain, A., Abbeel, P.: Denoising diffusion probabilistic models. *Advances in neural information processing systems* **33**, 6840–6851 (2020)
15. Hoffmann, M., Hoopes, A., Greve, D.N., Fischl, B., Dalca, A.V.: Anatomy-aware and acquisition-agnostic joint registration with synthmorph. *Imaging Neuroscience* (2024)
16. Holland, D., Dale, A.M., Initiative, A.D.N., et al.: Nonlinear registration of longitudinal images and measurement of change in regions of interest. *Medical image analysis* **15**(4), 489–497 (2011)
17. Hoopes, A., Hoffmann, M., Fischl, B., Gutttag, J., Dalca, A.V.: Hypermorph: Amortized hyperparameter learning for image registration. In: *Information Processing in Medical Imaging: 27th International Conference, IPMI 2021, Virtual Event, June 28–June 30, 2021, Proceedings 27*. pp. 3–17. Springer (2021)
18. Hua, X., Ching, C.R., Mezher, A., Gutman, B.A., Hibar, D.P., Bhatt, P., Leow, A.D., Jack Jr, C.R., Bernstein, M.A., Weiner, M.W., et al.: Mri-based brain atrophy rates in adni phase 2: acceleration and enrichment considerations for clinical trials. *Neurobiology of aging* **37**, 26–37 (2016)
19. Hua, X., Leow, A.D., Parikshak, N., Lee, S., Chiang, M.C., Toga, A.W., Jack Jr, C.R., Weiner, M.W., Thompson, P.M., Initiative, A.D.N., et al.: Tensor-based morphometry as a neuroimaging biomarker for alzheimer’s disease: an mri study of 676 ad, mci, and normal subjects. *Neuroimage* **43**(3), 458–469 (2008)
20. Jack Jr, C.R., Bernstein, M.A., Fox, N.C., Thompson, P., Alexander, G., Harvey, D., Borowski, B., Britson, P.J., L. Whitwell, J., Ward, C., et al.: The alzheimer’s disease neuroimaging initiative (adni): Mri methods. *Journal of Magnetic Resonance Imaging* **27**(4), 685–691 (2008)
21. Jian, B., Pan, J., Ghahremani, M., Rueckert, D., Wachinger, C., Wiestler, B.: Mamba? catch the hype or rethink what really helps for image registration. In: *International Workshop on Biomedical Image Registration*. pp. 86–97. Springer (2024)
22. Kim, B., Han, I., Ye, J.C.: Diffusemorph: Unsupervised deformable image registration using diffusion model. In: *European conference on computer vision*. pp. 347–364. Springer (2022)
23. Lachinov, D., Chakravarty, A., Grechenig, C., Schmidt-Erfurth, U., Bogunović, H.: Learning spatio-temporal model of disease progression with neuralodes from longitudinal volumetric data. *IEEE Transactions on Medical Imaging* (2023)
24. Lee, D., Alam, S., Jiang, J., Cervino, L., Hu, Y.C., Zhang, P.: Seq2morph: A deep learning deformable image registration algorithm for longitudinal imaging studies and adaptive radiotherapy. *Medical physics* **50**(2), 970–979 (2023)

25. Leow, A.D., Yanovsky, I., Chiang, M.C., Lee, A.D., Klunder, A.D., Lu, A., Becker, J.T., Davis, S.W., Toga, A.W., Thompson, P.M.: Statistical properties of jacobian maps and the realization of unbiased large-deformation nonlinear image registration. *IEEE transactions on medical imaging* **26**(6), 822–832 (2007)
26. Liu, Y., Chen, J., Wei, S., Carass, A., Prince, J.: On finite difference jacobian computation in deformable image registration. *International Journal of Computer Vision* pp. 1–11 (2024)
27. Marinescu, R.V., Oxtoby, N.P., Young, A.L., Bron, E.E., Toga, A.W., Weiner, M.W., Barkhof, F., Fox, N.C., Golland, P., Klein, S., et al.: Tadpole challenge: Accurate alzheimer’s disease prediction through crowdsourced forecasting of future data. In: *Predictive Intelligence in Medicine: Second International Workshop, PRIME 2019, Held in Conjunction with MICCAI 2019, Shenzhen, China, October 13, 2019, Proceedings 2*. pp. 1–10. Springer (2019)
28. Metz, C.T., Klein, S., Schaap, M., van Walsum, T., Niessen, W.J.: Nonrigid registration of dynamic medical imaging data using $nd + t$ b-splines and a groupwise optimization approach. *Medical image analysis* **15**(2), 238–249 (2011)
29. Modat, M., Ridgway, G.R., Taylor, Z.A., Lehmann, M., Barnes, J., Hawkes, D.J., Fox, N.C., Ourselin, S.: Fast free-form deformation using graphics processing units. *Computer methods and programs in biomedicine* **98**(3), 278–284 (2010)
30. Mok, T.C., Chung, A.: Fast symmetric diffeomorphic image registration with convolutional neural networks. In: *Proceedings of the IEEE/CVF conference on computer vision and pattern recognition*. pp. 4644–4653 (2020)
31. Mok, T.C., Chung, A.C.: Large deformation diffeomorphic image registration with laplacian pyramid networks. In: *Medical Image Computing and Computer Assisted Intervention–MICCAI 2020: 23rd International Conference, Lima, Peru, October 4–8, 2020, Proceedings, Part III 23*. pp. 211–221. Springer (2020)
32. Mok, T.C., Chung, A.C.: Conditional deformable image registration with convolutional neural network. In: *Medical Image Computing and Computer Assisted Intervention (MICCAI)*. pp. 35–45. Springer (2021)
33. Nestor, S.M., Rupsingh, R., Borrie, M., Smith, M., Accomazzi, V., Wells, J.L., Fogarty, J., Bartha, R., Initiative, A.D.N.: Ventricular enlargement as a possible measure of alzheimer’s disease progression validated using the alzheimer’s disease neuroimaging initiative database. *Brain* **131**(9), 2443–2454 (2008)
34. Ott, B.R., Cohen, R.A., Gongvatana, A., Okonkwo, O.C., Johanson, C.E., Stopa, E.G., Donahue, J.E., Silverberg, G.D., Initiative, A.D.N., et al.: Brain ventricular volume and cerebrospinal fluid biomarkers of alzheimer’s disease. *Journal of Alzheimer’s disease* **20**(2), 647–657 (2010)
35. Pock, T., Urschler, M., Zach, C., Beichel, R., Bischof, H.: A duality based algorithm for tv-l 1-optical-flow image registration. In: *International Conference on Medical Image Computing and Computer-Assisted Intervention*. pp. 511–518. Springer (2007)
36. Qiu, A., Albert, M., Younes, L., Miller, M.I.: Time sequence diffeomorphic metric mapping and parallel transport track time-dependent shape changes. *NeuroImage* **45**(1), S51–S60 (2009)
37. Qiu, H., Qin, C., Schuh, A., Hammernik, K., Rueckert, D.: Learning diffeomorphic and modality-invariant registration using b-splines. In: *Medical Imaging with Deep Learning* (2021)
38. Ren, M., Dey, N., Styner, M., Botteron, K., Gerig, G.: Local spatiotemporal representation learning for longitudinally-consistent neuroimage analysis. *Advances in neural information processing systems* **35**, 13541–13556 (2022)

39. Reuter, M., Schmansky, N.J., Rosas, H.D., Fischl, B.: Within-subject template estimation for unbiased longitudinal image analysis. *Neuroimage* **61**(4) (2012)
40. Rombach, R., Blattmann, A., Lorenz, D., Esser, P., Ommer, B.: High-resolution image synthesis with latent diffusion models. In: *Proceedings of the IEEE/CVF conference on computer vision and pattern recognition*. pp. 10684–10695 (2022)
41. Rueckert, D., Sonoda, L.L., Hayes, C., Hill, D.L., Leach, M.O., Hawkes, D.J.: Non-rigid registration using free-form deformations: application to breast mr images. *IEEE transactions on medical imaging* **18**(8), 712–721 (1999)
42. Shen, D., Davatzikos, C.: Measuring temporal morphological changes robustly in brain mr images via 4-dimensional template warping. *NeuroImage* **21**(4), 1508–1517 (2004)
43. Simpson, I.J., Woolrich, M., Groves, A.R., Schnabel, J.A.: Longitudinal brain mri analysis with uncertain registration. In: *Medical Image Computing and Computer-Assisted Intervention–MICCAI 2011: 14th International Conference, Toronto, Canada, September 18–22, 2011, Proceedings, Part II 14*. pp. 647–654. Springer (2011)
44. Thirion, J.P.: Image matching as a diffusion process: an analogy with maxwell’s demons. *Medical image analysis* **2**(3), 243–260 (1998)
45. Tian, L., Greer, H., Kwitt, R., Vialard, F.X., San José Estépar, R., Bouix, S., Rushmore, R., Niethammer, M.: unigradicon: A foundation model for medical image registration. In: *International Conference on Medical Image Computing and Computer-Assisted Intervention*. pp. 749–760. Springer (2024)
46. Tian, L., Greer, H., Vialard, F.X., Kwitt, R., Estépar, R.S.J., Rushmore, R.J., Makris, N., Bouix, S., Niethammer, M.: Gradicon: Approximate diffeomorphisms via gradient inverse consistency. In: *Proceedings of the IEEE/CVF Conference on Computer Vision and Pattern Recognition*. pp. 18084–18094 (2023)
47. Vercauteren, T., Pennec, X., Perchant, A., Ayache, N.: Diffeomorphic demons: Efficient non-parametric image registration. *NeuroImage* **45**(1), S61–S72 (2009)
48. Wang, Y., Qiu, H., Qin, C.: Conditional deformable image registration with spatially-variant and adaptive regularization. In: *2023 IEEE 20th International Symposium on Biomedical Imaging (ISBI)*. pp. 1–5. IEEE (2023)
49. Wu, G., Wang, Q., Shen, D., Initiative, A.D.N., et al.: Registration of longitudinal brain image sequences with implicit template and spatial-temporal heuristics. *NeuroImage* **59**(1), 404–421 (2012)
50. Wu, N., Xing, J., Zhang, M.: Tlrn: Temporal latent residual networks for large deformation image registration. In: *International Conference on Medical Image Computing and Computer-Assisted Intervention*. pp. 728–738. Springer (2024)
51. Wu, Y., Dong, M., Jena, R., Qin, C., Gee, J.C.: Neural ordinary differential equation based sequential image registration for dynamic characterization. *arXiv preprint arXiv:2404.02106* (2024)
52. Yang, D., Li, H., Low, D.A., Deasy, J.O., El Naqa, I.: A fast inverse consistent deformable image registration method based on symmetric optical flow computation. *Physics in Medicine & Biology* **53**(21), 6143 (2008)
53. Yigitsoy, M., Wachinger, C., Navab, N.: Temporal groupwise registration for motion modeling. In: *Biennial International Conference on Information Processing in Medical Imaging*. pp. 648–659. Springer (2011)
54. Zhuo, Y., Shen, Y.: Diffusereg: Denoising diffusion model for obtaining deformation fields in unsupervised deformable image registration. In: *International Conference on Medical Image Computing and Computer-Assisted Intervention*. pp. 597–607. Springer (2024)

A Supplementary Materials

Fig. 7. Demonstration of the non-linear time information learned by *TimeFlow/-diff*. The first row visualizes the variance of the time-embedded UNet’s outputs $\hat{f}_\theta(I_m, I_f, t)$ in $t \in [0, 2]$. The second row shows the cosine similarity of the time-embedding vector within $t \in [0, 2]$. Both figures demonstrate that *TimeFlow/-diff* learns comprehensive, non-linear temporal deformations rather than simple linear scaling.

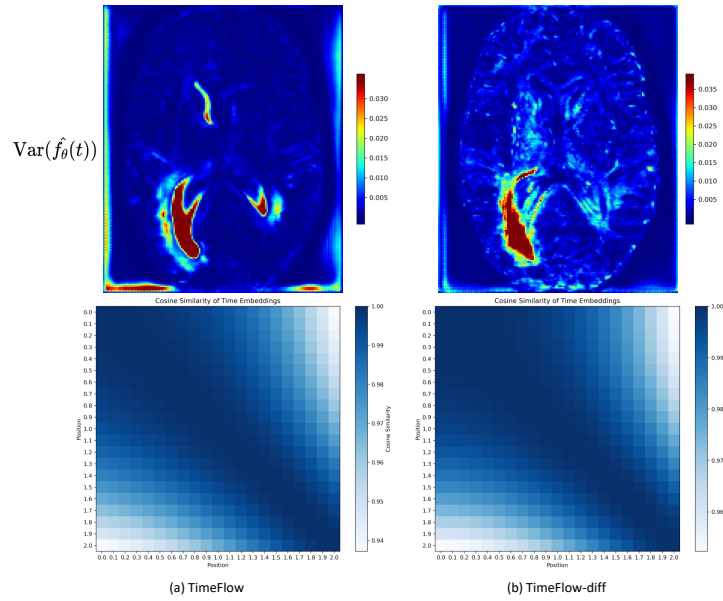


Table 3. Quantitative evaluation on pairwise registration between baseline visit and endpoint. The best score is marked in bold.

	MAE ↓	PSNR ↑	SDlogJ ↓	NDV(%) ↓
rigid	11.0±4.5	16.6±2.2	-	-
Seq-VXM	7.0±4.1	21.2±2.9	3.4±0.8	0.8±2.7
NODER	8.0±3.9	20.0±2.6	3.2±1.3	18.8±89.6
VXM	7.3±4.5	20.9±2.9	3.0±0.6	15.2±73.2
VXM _{diff}	6.7±3.7	21.6±2.9	4.3±1.3	33.9±175.8
TimeFlow	7.3±4.5	20.8±2.9	3.2±0.2	2.0±4.1
TimeFlow _{diff}	6.6±4.2	21.7±3.0	4.5±0.5	0.3±0.5